

Contents lists available at ScienceDirect

Ultramicroscopy

journal homepage: www.elsevier.com/locate/ultramic





Correlating electrochemical stimulus to structural change in liquid electron microscopy videos using the structural dissimilarity metric

Justin T. Mulvey^a, Katen P. Iyer^a, Tomàs Ortega^b, Jovany G. Merham^c, Yevheniy Pivak^d, Hongyu Sun^d, Allon I. Hochbaum^{a,c,e,f}, Joseph P. Patterson^{a,c,*}

- ^a Department of Material Science and Engineering, University of California-Irvine, Irvine, CA 92697, USA
- ^b Department of Electrical Engineering and Computer Science, University of California-Irvine, Irvine, CA 92697, USA
- Department of Chemistry, University of California, California-Irvine, Irvine, CA 92697, USA
- ^d DENSsolutions B.V., Informaticalaan 12, 2628 ZD Delft, the Netherlands
- e Department of Chemical and Biomolecular Engineering, University of California, California-Irvine, Irvine, CA 92697, USA
- f Department of Molecular Biology and Biochemistry, University of California, California-Irvine, Irvine, CA 92697, USA

ARTICLE INFO

Keywords: Structural dissimilarity Liquid cell transmission electron microscopy Structural similarity Electrochemistry Quantitative image analysis ImageJ

ABSTRACT

In-situ liquid cell transmission electron microscopy (LCTEM) with electrical biasing capabilities has emerged as an invaluable tool for directly imaging electrode processes with high temporal and spatial resolution. However, accurately quantifying structural changes that occur on the electrode and subsequently correlating them to the applied stimulus remains challenging. Here, we present structural dissimilarity (DSSIM) analysis as segmentation-free video processing algorithm for locally detecting and quantifying structural change occurring in LCTEM videos. In this study, DSSIM analysis is applied to two in-situ LCTEM videos to demonstrate how to implement this algorithm and interpret the results. We show DSSIM analysis can be used as a visualization tool for qualitative data analysis by highlighting structural changes which are easily missed when viewing the raw data. Furthermore, we demonstrate how DSSIM analysis can serve as a quantitative metric and efficiently convert 3-dimensional microscopy videos to 1-dimenional plots which makes it easy to interpret and compare events occurring at different timepoints in a video. In the analyses presented here, DSSIM is used to directly correlate the magnitude and temporal scale of structural change to the features of the applied electrical bias. ImageJ, Python, and MATLAB programs, including a user-friendly interface and accompanying documentation, are published alongside this manuscript to make DSSIM analysis easily accessible to the scientific community.

1. Introduction

In-situ liquid cell transmission electron microscopy (LCTEM) with biasing capabilities enables solution-state electrode processes to be recorded with nanoscale spatial resolution and millisecond-scale temporal resolution [1–5]. Direct observation of electric potential induced phenomena has contributed valuable mechanistic insights towards research in batteries, [6–9] catalysis, [10–13] and polymers [14,15]. The principal goal of many in-situ LCTEM electrochemical studies is to correlate the applied stimulus to structural changes captured in the video, such as material formation or dissolution. While structural changes may be visually apparent, raw LCTEM videos are often difficult to analyze for two main reasons. First, the liquid layer within the cell reduces object contrast in the images and introduces a large amount of

noise into the data [16]. As a result, subtle structural changes are easily missed when viewing the raw data. Second, LCTEM videos collected on high-framerate microscopes can reach 1000's of frames in size, resulting in multiple terabytes of data [17]. Manually identifying and comparing events in the raw data can be extremely time-consuming and subjective. Thus, large datasets require efficient video analysis algorithms to detect and measure structural change events so they can be easily interpreted and correlated to the applied stimulus.

The most common method of quantiatively analyzing structural change is with image segmentation algorithms, in which objects are identified and analyzed in every image of the video [18]. This has been widely used in the LCTEM community to quantify dynamic events such as micelle fusion [19], solid electrolyte interphase (SEI) layer growth [6], nanoparticle etching [20], and more [21]. However, in some

E-mail addresses: mulveyj@uci.edu (J.T. Mulvey), patters3@uci.edu (J.P. Patterson).

^{*} Corresponding author.

datasets which contain multiple classes of objects or continuous objects, segmentation can be highly subjective or impossible. Recently, there have been segmentation-free analysis algorithms developed to measure structural change without the need to label objects in the images [22]. For example, an algorithm was developed to quantify beam-induced damage over time while imaging organic thin-films [23]. This was accomplished by using the normalized cross-correlation metric to compare the first frame and subsequent frames of an electron dose-series. The success of this method for characterizing a dynamic process unsuitable for segmentation analysis demonstrates the need for continued development of segmentation-free metrics. Here, we present a new segmentation-free video analysis algorithm to highlight and quantify structural change using the structural dissimilarity (DSSIM) metric, a linear variant of the commonly used structural similarity (SSIM) metric [24].

DSSIM is an established measure of the perceived difference between two images, which compares local variation in the mean, standard deviation, and cross-correlation of pixel intensity values to produce a new dissimilarity image [25,26]. DSSIM was originally developed to assess the quality of structural information present in a reference and distorted image, such as comparing a raw image with a compressed image [25]. It was later adopted by the machine learning community as a metric to evaluate model performance by comparing a reconstructed image against a ground truth image [27]. The resulting dissimilarity image will highlight regions where the reconstruction image deviates the most from the ground truth image. To date, DSSIM has found several niche

applications for structural analysis in the microscopy community. For example, DSSIM/SSIM has been used to identify: neurochemical events from cyclic voltammetry, [28] microcalcification from mammography, [29] crack formation from X-ray tomography, [30] phase changes in polarized optical microscopy, [31] and dynamic behavior in confocal fluorescence microscopy [32]. A recent LCTEM study used the metric to quantify beam-induced gold nanoparticle growth because segmentation analysis was not possible [33]. To quantify growth, they used SSIM to compare pairs of images taken of the same region in the liquid cell before and after electron irradiation.

For the first time, we apply the DSSIM metric to spatially and temporally quantify the stimulated structural changes captured in LCTEM electrochemistry videos. The proposed DSSIM analysis video algorithm compares temporally offset frames of the input video to create a dissimilarity video, which measures and highlights locations where structural change has occurred. In Section 2, we describe how to apply and tune the parameters of DSSIM analysis. In Section 3, we analyze two in-situ LCTEM datasets from different studies and show it is possible to extract quantitative, easy-to-interpret information and gain additional insight into electrochemically-driven materials formation and dissolution. For each dataset, we demonstrate DSSIM analysis can be used to evaluate the correlation between the applied stimulus and the resulting structural change.

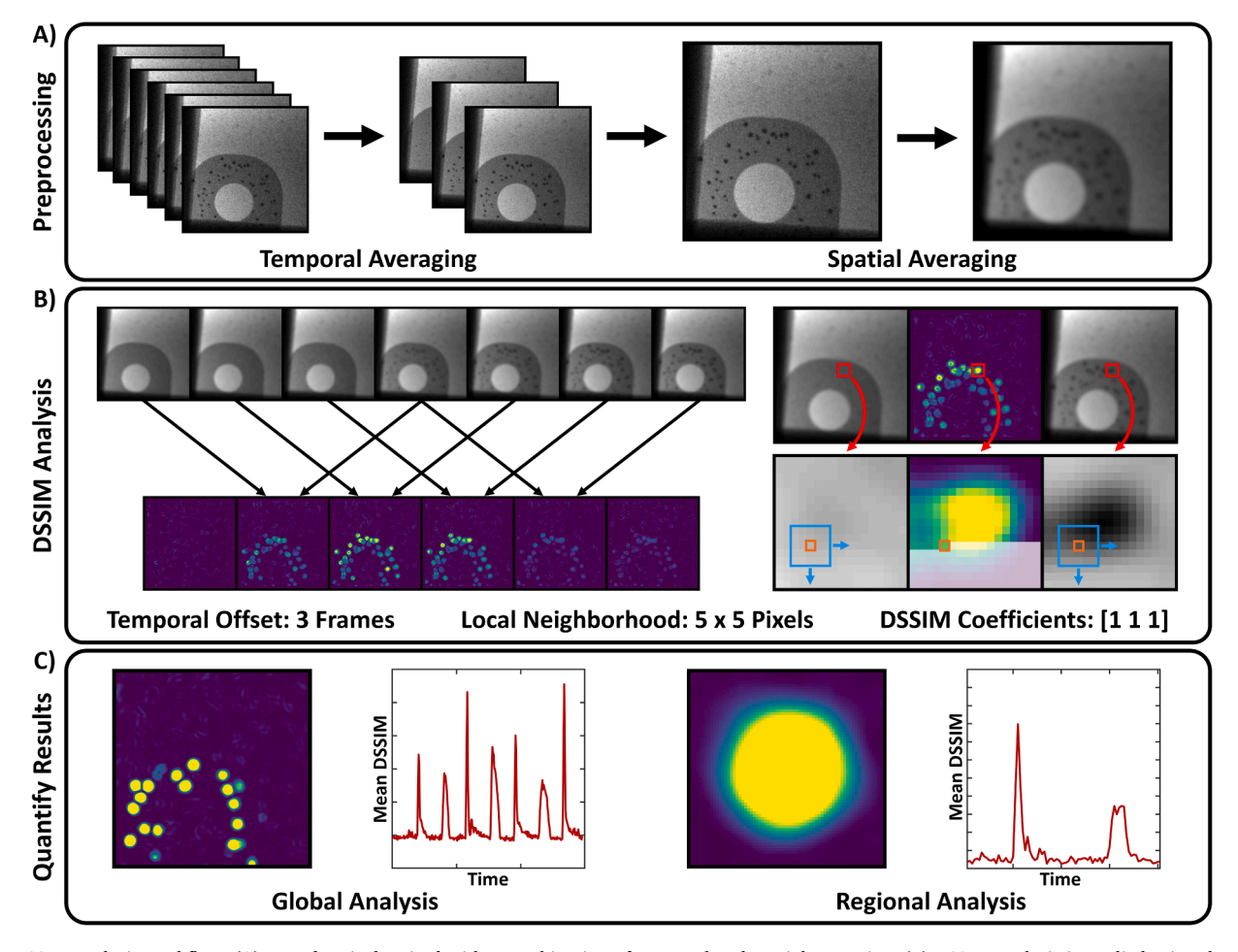


Fig. 1. DSSIM analysis workflow. (A) Raw data is denoised with a combination of temporal and spatial averaging. (B) DSSIM analysis is applied using the defined parameters. Temporally offset images in the video are compared in a sliding-window operation (left). Image pairs are analyzed with the DSSIM metric which compares the same local neighborhoods of each image to produce a DSSIM image (right). Note images have been downsized by a factor of 4 to improve figure legibility. (C) DSSIM analysis results are quantified with global analysis (entire image) and regional analysis (cropped image).

2. Methods

2.1. DSSIM analysis workflow

Fig. 1 describes the general workflow for applying DSSIM analysis to a video dataset. In step 1, the raw data is preprocessed to reduce noise in each frame prior to DSSIM analysis. In this study, noise is reduced by using frame averaging (temporal averaging) and Gaussian blurring (spatial averaging).

In step 2, DSSIM analysis is applied to the denoised video. The DSSIM analysis algorithm presented here is a sliding-window calculation which compares frame t with frame $t+\Delta t$ (Fig. 1B). First, the two frames are compared with the SSIM metric. For every pixel location in each pair of images (Fig. 1B, orange boxes), the metric compares intensity values in a Gaussian-weighted local neighborhood around the pixel location (Fig. 1B, blue boxes). Boarder pixels are excluded from the analysis. The Gaussian-weighted intensity values in the local neighborhoods are compared with three components: the mean (m), variance (v), and crosscorrelation (c) [26]. Then, these components are weighted by the exponents $[\alpha \beta \gamma]$ and multiplied together to produce a SSIM image (Eq. (1)). The SSIM image is linearly converted to a DSSIM image using Eq. (2). DSSIM values are between 0 and 1, where a high value corresponds to a region of high dissimilarity. The result of the sliding window algorithm is a DSSIM video, which is shorter than the input video by Δt frames.

$$SSIM(X_t, X_{t+\Delta t}) = m(X_t, X_{t+\Delta t})^{\alpha} * v(X_t, X_{t+\Delta t})^{\beta} * c(X_t, X_{t+\Delta t})^{\gamma}$$
(1)

$$DSSIM(X_{t}, X_{t+\Delta t}) = \frac{1 - SSIM(X_{t}, X_{t+\Delta t})}{2}$$
 (2)

There are 3 parameters that will affect the output of DSSIM analysis: the local neighborhood size, the temporal offset Δt , and the $[\alpha \ \beta \ \gamma]$ DSSIM coefficients. X_t and $X_{t+\Delta t}$ denote two local neighborhoods of common size (Fig. 1B, blue boxes) taken from the same pixel location (Fig. 1B, orange boxes) in both images. For example, the analysis shown in Fig. 1B uses 5×5 pixel local neighborhoods which are visualized with blue boxes. Every valid pair of neighborhoods is compared with DSSIM to construct the final dissimilarity image, and the size of the local neighborhood will determine the spatial resolution of the output. Δt is the temporal offset of the pair of frames and will determine the temporal resolution of the output. $[\alpha \ \beta \ \gamma]$ are the DSSIM coefficients which adjust the relative weighting of the mean, standard deviation, and cross-correlation components. Coefficients were kept at $[1\ 1\ 1]$ for the analyses presented here.

Lastly, the output of DSSIM analysis is quantified (Fig. 1C). The simplest method of quantification is calculating the global mean DSSIM value for each DSSIM image. This provides information about mean structural change occurring in the image, where high mean DSSIM values correspond to a high degree of structural change. Alternatively, it is often useful to perform regional analysis to compare structural change across different spatial locations in the data, [32] or to closely examine a particular event of interest. After quantification, the original 3-dimensional video is reduced to 1-dimensional data that is easily interpreted and correlated to other types of data.

2.2. Parameter tuning

The data analysis pipeline described here requires three parameters to be tuned in Step 2. While multiparameter analysis methods are generally considered to be complex, parameter tuning for DSSIM analysis is intuitive and directly related to the spatial and temporal resolution of the physical phenomena taking place. The spatial and temporal resolution of the detected dynamics will depend on the temporal offset and local neighborhood, respectively. Determining the ideal local neighborhood size requires consideration of the feature size of interest as well as the signal-to-noise ratio. In general, smaller neighborhoods

are ideal because they have the highest resolution and are most sensitive to small structural changes, but can result in artifacts and 'false events' caused by noise. If DSSIM analysis is applied to particle nucleation events, the neighborhood should be smaller than the particle (Fig. 1B). Typically, it is best to start parameter tuning with a large temporal offset and a large neighborhood to capture the most obvious dynamics. These parameters can then be iteratively decreased until the output becomes too noisy for clear interpretation. Depending on the nature of the dynamics, the user should focus on maximizing either temporal or spatial resolution. The structural change must occur over a time period that is strictly larger than twice the time of the temporal offset in order to be captured by DSSIM analysis (Nyquist-Shannon theorem). [34]

The DSSIM coefficients should generally be kept at [1 1 1]. However, it can be useful to remove one of the components of the DSSIM analysis by setting a coefficient to 0. For example, using coefficients [0 0 1] will reduce DSSIM to a local normalized cross-correlation calculation [35]. In the case of confocal fluorescence microscopy data, it was reported that the mean channel contributed mostly noise in the final output, so [0 1 1] coefficients were selected [32]. In the LCTEM datasets presented here, no exponent tuning was required.

Overall, we find parameter tuning to be intuitive and find that the end result is consistent and stable for a wide range of parameters. Additionally, it is important to note that DSSIM analysis is a computationally efficient algorithm that is easily parallelizable. This enables users to receive rapid feedback when tuning DSSIM analysis parameters.

2.3. Dataset considerations for DSSIM analysis

The DSSIM metric highlights both structural change and object movement. For datasets where both are occurring at the same time, DSSIM analysis will highlight both types of dynamics [32]. For structures that are in motion, object tracking and drift correction algorithms could be applied in the pre-processing steps to minimize movement from camera drift. This would enable the DSSIM metric to highlight structural changes. In the case of LCTEM electrochemical experiments, structures are typically attached to the electrode or the silicon nitride window, and so structural change can be isolated from object movement. In general, TEM imaging is better suited than scanning transmission electron microscopy (STEM) imaging for DSSIM analysis. This is because TEM images can be captured at higher framerates and there are no scanlines which result in artifacts after applying DSSIM analysis (Fig. 2C,E). In addition, near-zero pixel intensity values recorded in dark-field STEM imaging can cause instability in the DSSIM metric.

3. Results and discussion

3.1. DSSIM analysis of bright-field liquid cell STEM

DSSIM analysis is applied to a previously published bright-field liquid cell STEM video of SEI layer formation on a Pt electrode [6]. In this dataset, an electrochemical liquid cell was configured with Pt electrodes on a silicon nitride membrane to create an operando Li battery. Cyclic voltammetry (CV) was performed, in which the electrode potential was progressively decreased to induce charging, then progressively increased to induce discharging. During charging, the SEI layer rapidly grows on the electrode and there is a negative peak in the current (Fig. 2A-D, SI Video 1). During discharging, the SEI layer partially dissolves and there is a positive peak in the current (Fig. 2E,F, SI Video 1).

DSSIM analysis is applied to correlate the features of the recorded CV with the structural changes recorded on the electrode during charging and discharging. The dataset consists of 95 images taken across 402 s with a frame-time of 4.2 s. Preprocessing was done by applying a Gaussian blur with a first standard deviation of 90 nm (7 pixels) to remove noise. Due to the high signal-to-noise ratio and relatively low temporal resolution, no temporal averaging was applied to this dataset.

J.T. Mulvey et al. Ultramicroscopy 257 (2024) 113894

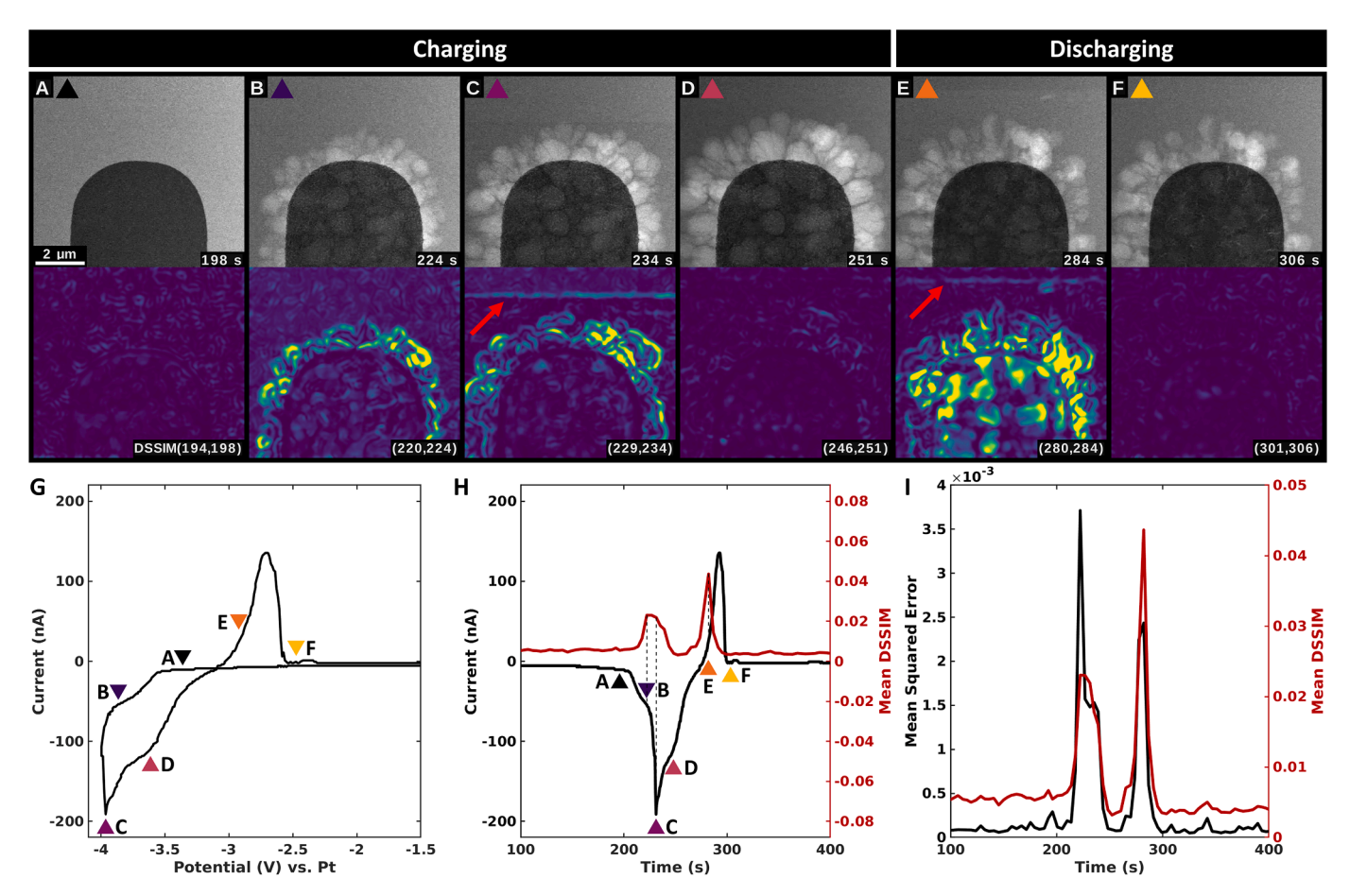


Fig. 2. DSSIM analysis applied to a previously published bright-field liquid cellSTEM video (SI Video 1) [6]. A-F) Select microscopy frames (top) and corresponding DSSIM frames (bottom) during electrode charging (A-D) and discharging (E,F). Bright pixels values correspond to regions of high dissimilarity between frames. Bottom labels correspond to the times of the two microscopy frames used to calculate the DSSIM image. Red arrows in (C, E) shows STEM scanline artifact in the DSSIM image. G) CV plotted as current vs. potential and H) current vs. time with key frames from (A-F) indicated with triangles. (H) contains a mean DSSIM plot, with key correlative features highlighted with dashed lines. High DSSIM values correspond to timepoints of high change. I) Mean DSSIM and MSE comparison.

Next, DSSIM analysis was applied with a local neighborhood of 244 \times 244 nm (19 \times 19 pixels), 1 frame offset, and [1 1 1] coefficients, resulting in 94 DSSIM frames.

The CV is shown as a current-potential plot in Fig. 2G and replotted as a current-time plot in Fig. 2H. The mean DSSIM value for each DSSIM frame is plotted to directly compare features of the current-time plot with the structural change taking place in the microscope. The analysis shows a clear correlation between the features of the CV and the resulting structural change. Interesting, there is a 9.0 s delay between the peak current and peak mean DSSIM during charging, and a 10.0 s delay between the negative peak current and peak mean DSSIM during discharging. The current value should be directly proportional to the rate of addition or removal of Li. Considering the frame-time of this dataset is 4.2 s, the mismatch represents 2 frames which could be attributed to a delay in recording the frames. The mismatch could also suggest the addition of Li during the peak current is not contributing to significant structural change of the SEI volume.

To compare the results of DSSIM with another metric, the analysis workflow described in Fig. 1 was applied but the DSSIM metric was replaced with the mean squared error (MSE) metric. Fig. 2I shows there is very good agreement between the timescale of features captured with both metrics. Fig. 2I also shows disagreement in relative peak heights of the two metrics during charging and discharging. This discrepancy is unsurprising, as disagreement between the two metrics has been previously reported [36–38]. MSE compares the absolute error between each pixel for the image pair, whereas DSSIM attempts to evaluate perceived differences in structure by comparing local regions of pixels.

As a result, DSSIM is less susceptible to single-pixel noise, which may be the reason for the disagreement in relative peak heights in Fig. 2I. Another key advantage of DSSIM analysis is the algorithm provides a map of local change for each pair of frames, which is not provided with MSE. This makes it easy to assess which regions of the image are contributing to the mean DSSIM value. Furthermore, the dissimilarity images can aid in qualitative analysis and reveal events easily missed. For example, Fig. 3 shows there is a subtle structural change that occurs a long time after motion has stopped elsewhere in the SEI layer.

3.2. DSSIM analysis of bright-field LCTEM

DSSIM analysis was applied to a bright-field LCTEM dataset which captures cyclic electrochemical Cu plating and stripping on a TiN_{x} electrode. An in-depth description of the electrode fabrication and experimental details will be released in an upcoming manuscript [39]. In this experiment, square-wave chronoamperometry was performed in which the electrode potential was decreased to -1.5~V (vs. TiN_{x}) and held constant to induce Cu plating, then instantaneously increased to +1.5~V (vs. TiN_{x}) and held constant to induce Cu stripping. Fig. 4A-D shows the first plating process as the dark Cu domains form on the electrode. Fig. 4E,F shows the first stripping process as the domains dissolve. In total, 4 plating and 3 stripping processes were performed (SI Video 2).

DSSIM analysis is applied to correlate the features of the square wave chronoamperometry data with the structural changes occurring on the electrode during plating and stripping. The raw dataset consists of 600

Fig. 3. (A,C) Consecutive frames in the bright-field liquid cell STEM video with (B) corresponding DSSIM image. Arrow in the DSSIM image highlights an isolated structural change event.

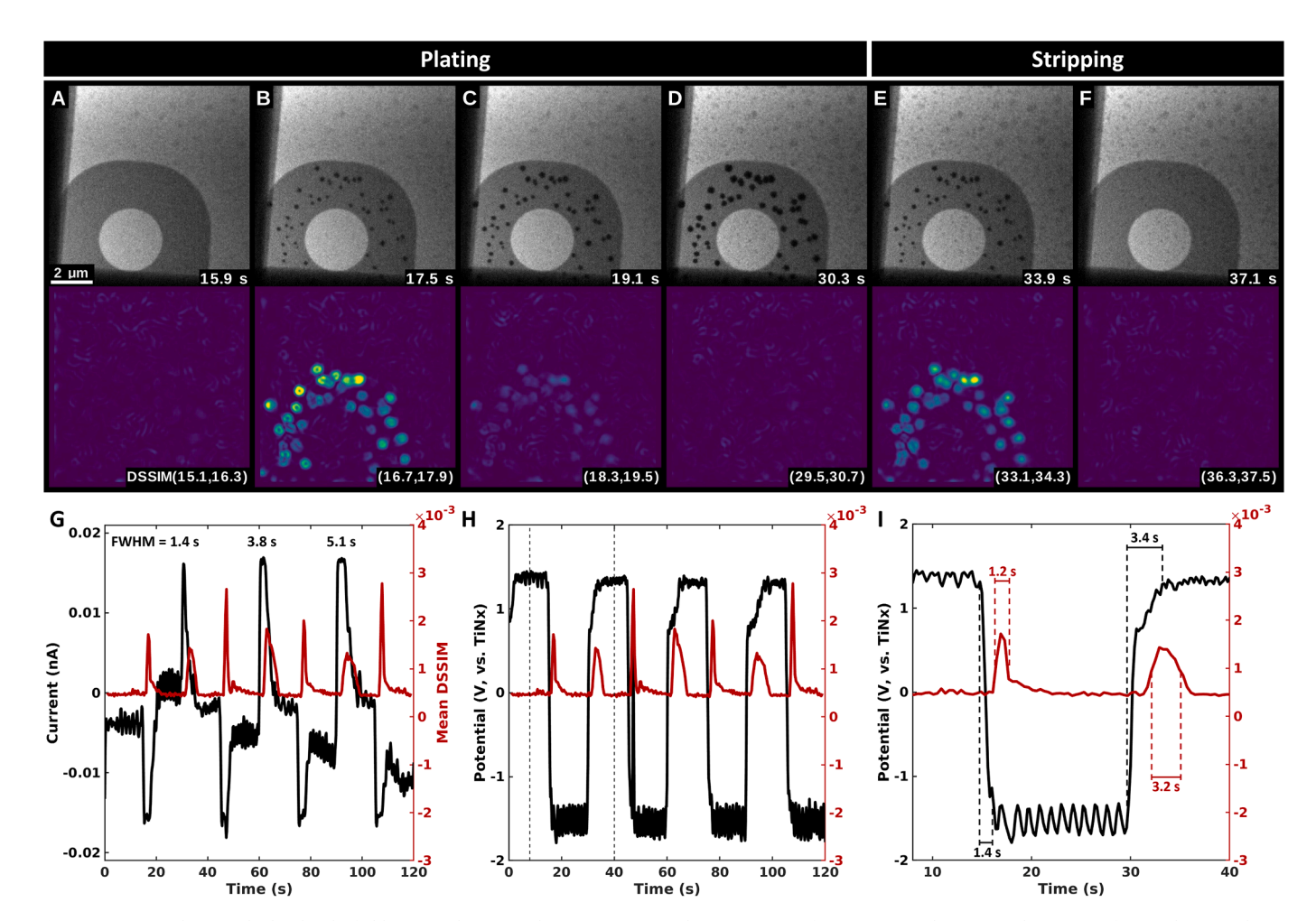


Fig. 4. DSSIM analysis applied to bright-field LCTEM data (SI Video 2). [39] A-F) Select microscopy frames (top) and corresponding DSSIM frames (bottom) during electrode plating (A-D) and stripping (E,F). Bright pixels values correspond to regions of high dissimilarity between frames. Bottom labels correspond to the times of the two microscopy frames used to calculate the DSSIM image. (G) Square-wave chronoamperometry plotted as current vs. time and (H) potential vs. time compared to mean DSSIM. High DSSIM values correspond to timepoints of high change. Current and potential data was smoothed using a Gaussian-weighted sliding-window average with a stand deviation of 1.5 datapoints. (I) Zoom-in to dashed region in H. Black dashed lines mark timescale of features in the potential plot. Red dashed lines mark the timescale of the DSSIM peaks using FWHM.

images taken across 120 s with a frame-time of 0.2 s. Preprocessing was done by first temporal averaging every 2 frames, reducing the size of the dataset to 300 frames. Next, a Gaussian blur was applied with a standard deviation of 120 nm (10 pixels) to remove noise. Then, DSSIM analysis was applied with a local neighborhood of 131 \times 131 nm (11 \times 11 pixels), 1.8 s offset (3 frames), and [1 1 1] coefficients. A frame offset of 3 was selected due to the high temporal resolution of the initial dataset, which meant there was little measurable change between adjacent

frames. These parameters resulted in 297 DSSIM frames.

The mean DSSIM is calculated for each frame and then plotted against the current-time data (Fig. 4G) and the potential-time data (Fig. 4H). The mean DSSIM plot shows that during plating, there is a sharp peak in Cu structural formations which subsequently slows down. During stripping, there is more uniform structural dissolution that occurs at a slower rate. This signature pattern is observed during each of the plating/stripping cycles captured in this dataset. Interestingly,

during stripping the DSSIM peaks show broadening across each subsequent cycle. This peak broadening is also seen via full-width half-max (FWHM) analysis of the stripping peaks in the current-time plot (Fig. 4G). These features in the chronoamperometry and mean DSSIM data suggest there is hysteresis across the stripping cycles. To further examine this, all DSSIM images were averaged together to display the entire history of structural change in a single image (Fig. 5). Fig. 5 shows there were regions that experienced multiple nucleation events (red arrows). This suggests there are some locations that favor Cu nucleation, or the Cu does not fully dissolve during stripping.

Closer examination of the potential-time and mean DSSIM plots from the first cycle shows there is a strong correlation between the shape of the square-wave chronoamperometry and the structural change events occurring on the electrode (Fig. 4I). During plating, the potential-time plot shows a delay of $1.4~\rm s$ before $-1.5~\rm V$ is reached. Applying FWHM analysis to the mean DSSIM peak shows that structural formation occurs across $1.2~\rm s$. During stripping, a similar phenomenon occurs in which there is a delay of $3.4~\rm s$ before the voltage reaches $+1.5~\rm V$. FWHM analysis of the mean DSSIM peak shows that structural dissolution occurs across $3.2~\rm s$. This analysis demonstrates the timescale of features in the square-wave chronoamperometry correlate with the timescale of structural change events occurring on the electrode.

3.3. Comparison of DSSIM analysis and segmentation analysis

Regional DSSIM analysis was applied to individual Cu plating and stripping events from the previously discussed bright-field LCTEM dataset (Section 3.2) to compare the results of DSSIM analysis to the results of segmentation-based growth rate analysis. Typically, particle growth rate is calculated by segmenting the particle in each frame and then calculating the derivative of area with respect to time [40] . Here, we compare growth rates calculated from segmentation analysis to the structural change calculated from regional DSSIM analysis.

Individual particle plating and stripping events from SI Video 2 were isolated and cropped for analysis (Fig. 6). For each frame, the particle area was calculated using a standard segmentation routine that has been described previously [40]. The green outline labels the edge of the segmented particle in each frame (Fig. 6A,D). Next, the particle growth rate was calculated by first smoothing the particle areas (Fig. 6B,E) and then taking the derivative of smoothed area with respect to time (Fig. 6C,F). The growth rate plots show a sharp increase in size during plating followed by a decrease in size during striping.

The same region was then cropped from the corresponding DSSIM frames and the mean DSSIM values were calculated. Fig. 6C,F shows the same features are captured in particle growth rate analysis and the regional mean DSSIM analysis. Fig. 6F shows DSSIM analysis correctly captures the subtle decrease in growth rate (dashed line). This

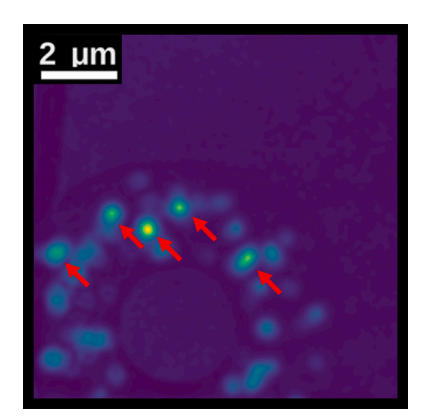


Fig. 5. Summation of all DSSIM frames from the bright-field LCTEM dataset (SI Video 2). Arrows highlight regions where multiple nucleation events occurred on the electrode.

demonstrates DSSIM can be used as an alternative to segmentation analysis in cases where the temporal scale and rate of structural change are of interest. It is important to highlight that DSSIM analysis provides different information than segmentation analysis. Specifically, DSSIM analysis will capture changes in object contrast, which are not directly captured in segmentation analysis. Additionally, DSSIM analysis will only provide relative information about how a structure is changing whereas segmentation analysis provides an absolute value about the particle size and position. For example, Fig. 6C,F shows the particle size is increasing steadily between 50 s and 60 s. While this slow growth is still visible in the DSSIM(47.5,48.7) images, the mean DSSIM graph does not highlight this processes. Note that increasing the temporal-offset of DSSIM analysis would improve the signal of the slow growth at the cost of temporal resolution. While particle segmentation is straightforward in the case presented here, DSSIM analysis can be applied to datasets in which segmentation is highly subjective or impossible, such as multiclass datasets where objects have a wide distribution of intensities [23, 32].

4. Code availability and efficiency

ImageJ, MATLAB, and Python code for applying DSSIM analysis is available via Github: github.com/JustinTMulvey/DSSIM_Analysis. DSSIM analysis is accessible as a MATLAB script, Python Jupyter notebook, or ImageJ plugin with an accompanying user-guide. The ImageJ plugin has an easy-to-use user-interface and can process floating-point and integer-type microscopy datasets (Fig. 7). The MATLAB and Python codes are parallelized and can process floating point videos data at 100–1000 MB/s (depending on neighborhood size) on a modern highend CPU (32 cores 3.5 GHz, 3200 MHz memory).

5. Conclusion

We have demonstrated DSSIM analysis can be used to detect and quantify structural change in LCTEM videos. We showed the method can be used to assist in qualitative analysis and reveal structural change that is easily missed when viewing the raw data. We also showed the algorithm can be used to quantitatively correlate the applied electrochemical biasing to the structural change that occurs on the electrode. We verified the accuracy of the metric by comparing it to segmentation analysis and found good agreement in temporal scale and magnitude of individual particle growth rates. Given the computation efficiency and ease of interpretation, we believe there is great potential to use DSSIM analysis for real-time event detection during data acquisition to highlight changes taking place to the microscope operator. This use case may also extend as an automated event detection algorithm for application in sparse imaging.

Data acquisition

The bright-field liquid cell STEM video of SEI layer formation on a Pt electrode was acquired by downloading the SI video from the publication. [6] The CV data was extracted and aligned to frames using a custom computer vision script. Frame times and CV times were estimated by matching the extracted frames to the publication figure time stamps and then using linear interpolation. The bright-field LCTEM dataset of Cu plating and stripping on a ${\rm TiN}_{\rm x}$ electrode and accompanying square wave chronoamperometry data was received as raw data [39].

Declaration of generative AI and AI-assisted technologies in the writing process

During the preparation of this work the authors used OpenAI's ChatGPT 3.0 in order to improve phrasing and clarity of the writing. After using this tool, the authors reviewed and edited the content as needed and take full responsibility for the content of the publication.

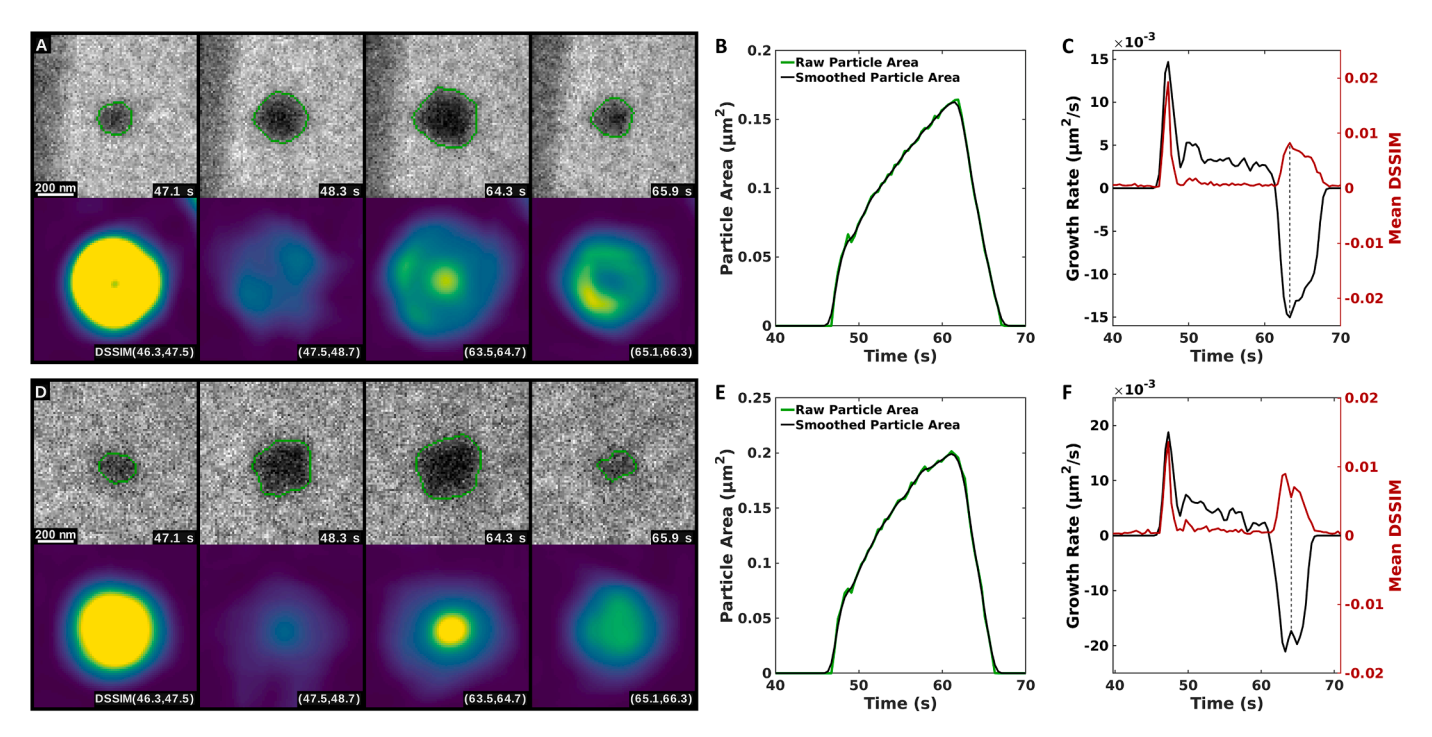


Fig. 6. Regional DSSIM analysis compared to segmentation-based growth-rate analysis. (A,D) Select microscopy frames showing segmentation of particle (top) and corresponding DSSIM frames (bottom) during electrode plating and stripping. Bright pixels values correspond to regions of high dissimilarity between frames. Bottom labels correspond to the times of the two microscopy frames used to calculate the DSSIM image. (B,E) Segmented particle areas for each frame plotted over time. Black line indicates a sliding-window Gaussian-weighted average. (C,F) Growth rate calculated as the derivative of the smoothed particle area with respect to time and mean DSSIM from regional analysis. Dashed lines show key features are aligned.

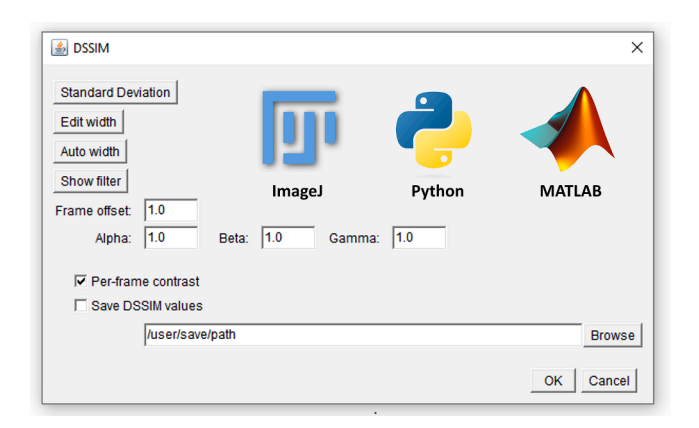


Fig. 7. ImageJ user interface for applying DSSIM analysis. DSSIM analysis can also be applied using Python or MATLAB scripts.

Declaration of Competing Interest

Y. Pivak and H. Sun work for DENSsolutions B.V., a company manufacturing and marketing in-situ TEM systems. The remaining authors have no conflicts to declare.

Data availability

Data will be made available upon reasonable request.

Acknowledgments

This research was primarily supported by the National Science Foundation Materials Research Science and Engineering Center program through the UC Irvine Center for Complex and Active Materials (DMR- 2011967). The authors acknowledge the use of facilities and instrumentation at the UC Irvine Materials Research Institute (IMRI) supported in part by the National Science Foundation Materials Research Science and Engineering Center program through the UC Irvine Center for Complex and Active Materials (DMR-2011967).

Supplementary materials

Supplementary material associated with this article can be found, in the online version, at doi:10.1016/j.ultramic.2023.113894.

References

- N. De Jonge, F.M. Ross, Electron microscopy of specimens in liquid, Nat. Nanotechnol. 6 (2011) 695–704.
- [2] F.M. Ross, Opportunities and challenges in liquid cell electron microscopy, Science 350 (2015) aaa9886.
- [3] U. Mirsaidov, J.P. Patterson, H. Zheng, Liquid phase transmission electron microscopy for imaging of nanoscale processes in solution, MRS Bull. 45 (2020) 704–712.
- [4] J. Sung, et al., Liquid-phase transmission electron microscopy for reliable in situ imaging of nanomaterials, Annu. Rev. Chem. Biomol. Eng. 13 (2022) 167–191.
- [5] P. Abellan, T.J. Woehl, Liquid cell electron microscopy for the study of growth dynamics of nanomaterials and structure of soft matter, in: C.S.S.R. Kumar (Ed.), In-situ Characterization Techniques For Nanomaterials, Springer, Berlin Heidelberg, 2018, pp. 1–31, https://doi.org/10.1007/978-3-662-56322-9_1.
- [6] B.L. Mehdi, et al., Observation and quantification of nanoscale processes in lithium batteries by operando electrochemical (S)TEM, Nano Lett. 15 (2015) 2168–2173.
- [7] S.-Y. Lee, et al., Unveiling the mechanisms of lithium dendrite suppression by cationic polymer film induced solid–electrolyte interphase modification, Energy Environ. Sci. 13 (2020) 1832–1842.
- [8] B.L. Mehdi, et al., The impact of Li grain size on coulombic efficiency in Li batteries, Sci. Rep. 6 (2016) 34267.
- [9] A.J. Leenheer, K.L. Jungjohann, K.R. Zavadil, J.P. Sullivan, C.T. Harris, Lithium Electrodeposition dynamics in aprotic electrolyte observed in Situ via transmission electron microscopy, ACS Nano 9 (2015) 4379–4389.
- [10] Y. Yang, et al., Operando methods in electrocatalysis, ACS Catal. 11 (2021) 1136–1178.
- [11] S. Hwang, X. Chen, G. Zhou, D. Su, In Situ transmission electron microscopy on energy-related catalysis, Adv. Energy Mater. 10 (2020), 1902105.

- [12] Y. Pan, X. Li, D. Su, Understanding the structural dynamics of electrocatalysts via liquid cell transmission electron microscopy, Curr. Opin. Electrochem. 33 (2022), 100936
- [13] Y. Yang, et al., Operando studies reveal active Cu nanograins for CO2 electroreduction, Nature 614 (2023) 262–269.
- [14] J. Liu, et al., Direct imaging of the electrochemical deposition of poly(3,4-ethylenedioxythiophene) by transmission electron microscopy, ACS Macro Lett. 4 (2015) 897–900.
- [15] V. Subramanian, D.C. Martin, In situ observations of nanofibril nucleation and growth during the electrochemical polymerization of poly(3,4ethylenedioxythiophene) using liquid-phase transmission electron microscopy, Nano Lett. 21 (2021) 9077–9084.
- [16] N. de Jonge, L. Houben, R.E. Dunin-Borkowski, F.M. Ross, Resolution and aberration correction in liquid cell transmission electron microscopy, Nat. Rev. Mater. 4 (2019) 61–78.
- [17] Spurgeon, S.R. Towards data-driven next-generation transmission electron microscopy. Nat. Mater. 6.
- [18] A. Rizvi, J.T. Mulvey, B.P. Carpenter, R. Talosig, J.P. Patterson, A close look at molecular self-assembly with the transmission electron microscope, Chem. Rev. (2021), https://doi.org/10.1021/acs.chemrev.1c00189.
- [19] L.R. Parent, et al., Directly observing micelle fusion and growth in solution by liquid-cell transmission electron microscopy, J. Am. Chem. Soc. 139 (2017) 17140–17151.
- [20] C. Yan, et al., Facet-selective etching trajectories of individual semiconductor nanocrystals, Sci. Adv. 8 (2022) eabq1700.
- [21] L. Yao, Z. Ou, B. Luo, C. Xu, Q. Chen, Machine learning to reveal nanoparticle dynamics from liquid-phase TEM videos, ACS Cent. Sci. 6 (2020) 1421–1430.
- [22] S. Reehl, et al., Event detection for undersampled electron microscopy experiments: a control chart case study, Qual. Eng. 32 (2020) 244–254.
- [23] Z.J.W.A. Leijten, A.D.A. Keizer, G. de With, H. Friedrich, Quantitative analysis of electron beam damage in organic thin films, J. Phys. Chem. C 121 (2017) 10552–10561.
- [24] A. Loza, L. Mihaylova, N. Canagarajah, D. Bull, Structural similarity-based object tracking in video sequences, in: 2006 9th International Conference on Information Fusion 1–6, IEEE, 2006, https://doi.org/10.1109/ICIF.2006.301574.
- [25] Z. Wang, A.C. Bovik, H.R. Sheikh, E.P. Simoncelli, Image quality assessment: from error visibility to structural similarity, IEEE Trans. Image Process. 13 (2004) 600–612.

- [26] D.M. Rouse, S.S. Hemami, Understanding and simplifying the structural similarity metric, in: 2008 15th IEEE International Conference on Image Processing 1188–1191, IEEE, 2008, https://doi.org/10.1109/ICIP.2008.4711973.
- [27] Y. Wu, et al., Three-dimensional virtual refocusing of fluorescence microscopy images using deep learning, Nat. Methods 16 (2019) 1323–1331.
- [28] P. Puthongkham, et al., Structural similarity image analysis for detection of adenosine and dopamine in fast-scan cyclic voltammetry color plots, Anal. Chem. 92 (2020) 10485–10494.
- [29] A. Touil, K. Kalti, P.-H. Conze, B. Solaiman, M.A. Mahjoub, Automatic detection of microcalcification based on morphological operations and structural similarity indices, Biocybern. Biomed. Eng. 40 (2020) 1155–1173.
- [30] D. Ushizima, T. Perciano, D. Parkinson, Fast Detection of Material Deformation Through Structural Dissimilarity, IEEE, 2015, https://doi.org/10.1109/ bigdata.2015.7364080.
- [31] B.T.P. Madhav, M. Venu Gopala Rao, V.G.K.M Pisipati, Identification of liquid crystalline phases in 7O.09 compound based on structural similarity index measure, Liq. Cryst. 42 (2015) 198–203.
- [32] S. Selmani, et al., Electrically fueled active supramolecular materials, J. Am. Chem. Soc. (2022), https://doi.org/10.1021/jacs.2c01884.
- [33] L.A. Bultema, et al., The effect of secondary electrons on radiolysis as observed by in liquid TEM: the role of window material and electrical bias, Ultramicroscopy 240 (2022), 113579.
- [34] C.E. Shannon, Communication in the presence of noise, Proc. IRE 37 (1949) 10-21.
- [35] G. Prieto, E. Guibelalde, M. Chevalier, A. Turrero, Use of the cross-correlation component of the multiscale structural similarity metric (R* metric) for the evaluation of medical images: R* metric for the evaluation of medical images, Med. Phys. 38 (2011) 4512–4517.
- [36] M. Ederer, S. Löffler, Image difference metrics for high-resolution electron microscopy, Ultramicroscopy 240 (2022), 113578.
- [37] J. Nilsson, T. Akenine-Möller, Understanding SSIM, 2020. Preprint at, http://arxiv. org/abs/2006.13846.
- [38] Zhou Wang, A.C Bovik, Mean squared error: love it or leave it? A new look at Signal Fidelity Measures, IEEE Signal Process, Mag. 26 (2009) 98–117.
- [39] Park, J. et al. Metal plating and stripping on a titanium nitride microelectrode: an electrochemical transmission electron microscopy study.
- [40] A. Rizvi, J.T. Mulvey, J.P. Patterson, Observation of liquid-liquid-phase separation and vesicle spreading during supported bilayer formation via liquid-phase transmission electron microscopy, Nano Lett. 21 (2021) 10325–10332.